Editors' Suggestion

Unified description of interactions and energy loss of particles in dense matter and plasmas

C. D. Archubi [*] and N. R. Arista [†]

Consejo Nacional de Investigaciones Científicas y Técnicas - Universidad de Buenos Aires, Instituto de Astronomía y Física del Espacio, Pabellón IAFE, 1428 Buenos Aires, Argentina;

Universidad de Buenos Aires, Facultad de Ciencias Exactas y Naturales, Departamento de Física, Ciudad Universitaria, 1428 Buenos Aires, Argentina;

and Centro Atómico Bariloche and Instituto Balseiro, Comisión Nacional de Energía Atómica, 8400 S. C. de Bariloche, Argentina

(Received 14 August 2020; accepted 21 October 2020; published 13 November 2020)

In this work, we propose a unified model to evaluate processes of electronic interactions of charged particles with hot and dense matter, including energy losses, mean free paths, and thermalization ranges of protons or other light ions. To formulate this method, we introduce modifications to the extended-wave-packet method, which allows one to describe and evaluate the effects of ionization as well as changes in target density and temperature. The ionization of the target leads to the formation of a dense surrounding plasma with distinct energy-absorption properties. We use this unified method to evaluate the contributions of inner shells and free electrons (produced by the target ionization) to the energy loss of protons in Si, C, and Fe targets, on an extensive range of parameters that include low, intermediate, and high energies, with densities and temperatures going from normal laboratory conditions to very high values, such as those of interest for inertial fusion and astrophysical studies.

DOI: 10.1103/PhysRevA.102.052811

I. INTRODUCTION

The interaction of energetic particles with matter subject to extreme conditions of densities and temperatures is a subject of great interest and relevance in different areas of research, such as current developments on magnetic and inertial fusion, as well as in studies of various astrophysical environments. In particular, interaction processes in materials such as carbon, silicon, and iron are some of the typical and common cases of interest in those studies.

Within the field of magnetic fusion research, elements currently tested as appropriate materials for first-wall or divertor components in Tokamak devices (plasma-facing materials), including the International Thermonuclear Experimental Reactor (ITER) project, consider graphite, Fe, and C and Si composites, among other elements [1–3]. The effect of intense irradiation (sputtering) of these materials by protons, deuterons, or alpha particles is a subject of central interest for magnetic fusion research [2,4].

In addition, C, Al, Si, and related composites are among a list of currently studied elements considered for possible use in inertial-confinement fusion (ICF) devices [5–9]. These studies require a precise knowledge of the properties of various materials on a very wide range of densities and temperatures. In particular, the range of densities from 10^{15} to 10^{25} particles per cm^3 and temperatures from tens of eV to tens of keV are within the range of interest for these studies [10,11]. Numerous studies of irradiation of various targets with light and heavy ions as well as ion clusters have been made [12–24].

In a very different area, C, Si, and Fe are of central interest in studies of stellar interiors, such as in the cases of giant stars or white dwarfs. Thus, for instance, carbon and silicon burning in massive stars are important stages in the process of stellar evolution [25,26]. The ranges of densities and temperatures of interest for these studies are extremely wide. Core conditions in massive stars evolve from central densities rising from 10^5 to 10^9 g/cm^3, and temperatures in the range of 10^8–10^9 K, as the processes of C, O, Ne, and Si burn take place [27], with a chain of processes ending up in iron-rich stars, as a nearly final stage previous to a supernova explosion [25,26]. By similar considerations, dwarf stars may also be considered, restricting our calculations to the nonrelativistic regime in the case of white dwarfs [27,28]. (The less extreme cases of brown or red dwarfs are also within the general coverage of the present approach.) Considering the typical speeds of electrons in dense plasmas, a relativistic limit may be estimated in the range of temperatures of $\sim 10^9$ K and electron densities of $\sim 10^{29}$ cm^{-3} (equivalent to mass densities of $\sim 3 \times 10^5$ g/cm^{-3} for carbon-rich stars).

There has not been a unified theoretical framework to describe the interaction of charged particles with matter under such diverse conditions, and therefore different approaches are usually combined. The main purpose of this study is to present a unified description that may be applied to the wide range of conditions described before. Our model includes the description of electronic excitations produced on both atomic shells and on the surrounding plasma of free electrons, under conditions of high densities and temperatures. To show the range of applicability of this approach, we will apply it to

[*] archubi@iafe.uba.ar
[†] arista@cab.cnea.ar

several cases of interest that span the wide range of conditions described above.

The use of dielectric-function models to describe the interactions and energy-loss processes of particles in matter has a long and very rich history. Starting with the pioneering work of Lindhard [29] and Ritchie [30], the use of these models to describe inelastic interactions became one of the most useful methods in this area. However, these models were built on the assumption of a free-electron gas, most appropriate to the case of conduction or valence electrons. More elaborate models that extend the applicability to inner shells make use of the *shellwise local plasma approximation*, showing good agreement with experiments. A comprehensive review of this method was recently presented in Ref. [31], where reference to previous work is made. Alternative models based on semiclassical assumptions were also developed to describe classical and quantum plasmas [32–35]. Additionally, the interaction of charged particles with plasmas of arbitrary degeneracy was studied [36–39].

A further extension of the dielectric-function approach was made by Kaneko, who in a series of papers [40–42] developed the *wave-packet model* (WPM) of dielectric response to describe, in a very general way, the ionization of atomic shells. More recently, we have extended Kaneko's wave-packet model in order to include the effects of binding energies of the various shells [43–45]; the result of this previous study is called the *extended-wave-packet model* (EWPM). In the present study, we reformulate the EWPM in order to describe both bound and free plasma electrons under conditions of thermal equilibrium. This will provide us with a second extension of the wave-packet model. Since this formulation covers all the usual states of matter, i.e., atoms, ions, solids and plasmas, we refer to this approach as the *unified wave-packet model* (UWPM).

After formulating the model in a general way, we will consider some particular cases in the interaction of energetic protons with three typical elements, i.e., C, Si, and Fe, under rather extreme conditions of densities and temperatures, as well as highly ionized plasmas in typical stellar interiors, showing in particular the effects of changes in density, temperature, and ionization state.

The paper is organized as follows. In Sec. II, a summary of the dielectric model for a free-electron gas in thermal equilibrium is presented. In Sec. III, the WPM approach is briefly described together with our extension that considers the binding energy for each electronic shell of the target (EWPM). A further and different extension is presented in Sec. IV for hot quantum plasmas, completing our so-called unified wave-packet model (UWPM). In Sec. V, experimental and theoretical results from calculations are discussed for a wide variety of cases, from cold solid targets to hot stellar regions. Finally, conclusions are summarized in Sec. VI.

II. DIELECTRIC FUNCTION OF QUANTUM PLASMAS

The response of the free plasma electrons to an external perturbation may be treated following the original analyses made by Lindhard [29] and Ritchie [30] for a charged particle traveling through a free-electron gas. These original treatments were restricted to the case of a degenerate plasma with temperature $T = 0$; however, the same analysis using quantum mechanical perturbation theory can be made for the case of dense plasmas in thermal equilibrium [38], using the most general expression for the dielectric function,

$$\epsilon(k,\omega) = 1 + \frac{e^2}{\pi^2 k^2}\int d^3k' \, \frac{f(\overrightarrow{k}+\overrightarrow{k'}) - f(\overrightarrow{k'})}{\hbar\omega + i\delta - (E_{\overrightarrow{k}+\overrightarrow{k'}} - E_{\overrightarrow{k'}})}, \tag{1}$$

where $E_{\overrightarrow{q}} = \hbar^2 q^2/2m$, and $f(\overrightarrow{k})$ is the Fermi-Dirac distribution function for plasmas of arbitrary degree of degeneracy,

$$f(\overrightarrow{k}) = \{1 + \exp[\beta(E_k - \mu)]\}^{-1}, \tag{2}$$

where $\beta = 1/k_B T$, $E_k = \hbar^2 k^2/2m$, and μ is the chemical potential of the plasma, with electron density n and temperature T. The chemical potential may be calculated with the Fermi-Dirac integral of order 1/2 using Eq. (6) of Ref. [38].

Classical and semiclassical results for the dielectric function are obtained from this expression for the long-wavelength and low-frequency limit, making the following approximations: $\overrightarrow{k} \to 0$, $f(\overrightarrow{k}+\overrightarrow{k'}) - f(\overrightarrow{k'}) \cong \overrightarrow{k}\cdot\overrightarrow{\nabla}_{k'} f(\overrightarrow{k'}) = \hbar\overrightarrow{k}\cdot\overrightarrow{v}(\partial f/\partial E)$, and $E_{\overrightarrow{k}+\overrightarrow{k'}} - E_{\overrightarrow{k'}} \cong \overrightarrow{k}\cdot\overrightarrow{\nabla}_{k'} E_{k'} = \hbar\overrightarrow{k}\cdot\overrightarrow{v}$.

From Eq. (1), the integral for the imaginary part of the dielectric function can be made in an exact way for all degrees of degeneracy and yields [38]

$$\varepsilon_2(k,\omega) \cong \frac{\pi\chi_0^2}{8z^3}\theta \, \ln\left\{\frac{1+\exp[\eta - D(u-z)^2]}{1+\exp[\eta - D(u+z)^2]}\right\}, \tag{3}$$

where $\chi_0^2 = 1/\pi k_F a_0$, $\theta = k_B T/E_F$, $D = 1/\theta$, $\eta = \beta\mu = \mu/k_B T$, $u = \omega/kv_F$, $z = k/2k_F$, with $E_F = \hbar^2 k_F^2/2m$ the Fermi energy and k_F the corresponding wave vector, and where a_0 is the Bohr radius and k_B is Boltzmann's constant.

In the limit of high temperatures, where the restrictions imposed by the Pauli principle may be neglected, $\varepsilon_2(k,\omega)$ takes the form [38]

$$\varepsilon_2(k,\omega) \cong \frac{\pi\chi_0^2}{8z^3}\theta \, e^{\eta}\left[e^{-D(u-z)^2} - e^{-D(u+z)^2}\right] \tag{4}$$

and the factor e^{η} is approximated by

$$e^{\eta} \cong \frac{4}{3\sqrt{\pi}}\frac{1}{\theta^{3/2}}, \tag{5}$$

which leads to

$$\varepsilon_2(k,\omega) \cong \frac{\sqrt{\pi}}{6}\frac{\chi_0^2}{\theta^{1/2}z^3}\left[e^{-D(u-z)^2} - e^{-D(u+z)^2}\right]. \tag{6}$$

It should be noticed that this expression still contains the quantum behavior usually characterized as the Bethe ridge, which arises around the line $u = z$ (in the u-z plane), corresponding to the condition $\omega = \hbar k^2/2m$; i.e., energy transfer in single-particle excitations [29,30,38]. Therefore, this provides a correct description of short-range excitations and eliminates the need to introduce a cutoff when integrating the total-energy loss as is required by the classical or semiclassical descriptions [34,35].

The real part of the dielectric function may be obtained from $\varepsilon_2(k,\omega)$ using the Kramers-Kronig relations. Explicit integral forms and approximations are given in Ref. [38].

Finally, the *energy-loss function* is defined as

$$F(k,\omega) = \mathrm{Im}\left[\frac{-1}{\epsilon(k,\omega)}\right], \tag{7}$$

which is used to describe a process of energy transfer $\hbar\omega$ and momentum transfer $\hbar\vec{k}$ to the electron gas.

The analysis of the energy-loss function can be made through approximative solutions of the so-called Fermi-Dirac integrals for different limits and leads to specific quantum mechanical expressions for low temperatures, where the restrictions produced by the Pauli principle becomes relevant, and for high temperatures, where connections with classical results can be made.

For the particular limit of low frequencies and high temperatures, the energy-loss function obtained from the quantum treatment yields the following expression [38]:

$$F(k,\omega) \cong \frac{nm^2e^2k\omega}{(k^2+k_D^2)^2}\left[\frac{2\pi}{mk_BT}\right]^{3/2}\exp\left[\frac{-\hbar^2k^2}{8mk_BT}\right], \tag{8}$$

where $k_D = \omega_p(m/k_BT)^{1/2}$ is the Debye screening constant. This expression differs from the corresponding classical result by the exponential term, which produces a gradual fading of the interactions with high momentum transfers (i.e., a gradual cutoff of high-k values).

This expression will be used later on to obtain an analytical approximation for the low-energy stopping power.

III. KANEKO'S WAVE-PACKET MODEL

In our unified model, the contribution of bound states to the target response is calculated using our extension of the wave-packet model [43–45]. The approach has been developed for targets at $T = 0$ and assumes that the population of each atomic shell corresponds to the maximum number N_s of electrons associated to the shell in the ground state. The most important assumption is the consideration of Gaussian distributions for the electron velocities of the atomic shells, namely, $f(v) \sim e^{-v^2/\overline{v}^2}$, where $\overline{v}$ is a characteristic speed of the considered shell. The dielectric function for this system is described according to the Kaneko's model [40–42] in terms of a characteristic wave vector $\overline{q}$, which is related to $\overline{v}$ by $\hbar\overline{q} = m\overline{v}$, where m is the electron mass. The value of $\overline{q}$ is determined by the relation $\overline{q} = q_1N_s^{1/3}$, where q_1 is a shell parameter whose value is determined from Hartree-Fock calculations of electron-velocity distributions using the results of previous authors [46,47].

A. Dielectric function

By assuming Gaussian distributions of electron speeds, the wave-packet model yields closed analytical expressions for the real and imaginary parts of the dielectric function $\epsilon(k,\omega) = \epsilon_1(k,\omega) + i\epsilon_2(k,\omega)$, where k and ω are the wave-vector and frequency variables. The results for ϵ_1 and ϵ_2 may be cast in a convenient way in terms of the dimensionless variables $u' = \omega/k\overline{v}$ and $z' = k/2\overline{q}$ (which are analogous to the Lindhard's u, z variables), as follows [40]:

$$\epsilon_1(u',z') = 1 + \frac{\chi^2}{8}\frac{1}{z'^3}[G(u'+z') - G(u'-z')], \tag{9}$$

$$\epsilon_2(u',z') = \frac{\pi\chi^2}{8}\frac{1}{z'^3}\left[e^{-(u'-z')^2} - e^{-(u'-z')^2}\right], \tag{10}$$

with a parameter $\chi^2 = e^2/\pi\hbar\overline{v}$.

The function $G(x)$ is defined by

$$G(x) = 2\sqrt{\pi}x\int_0^1 e^{(t^2-1)x^2}dt. \tag{11}$$

Although this dielectric function was originally proposed by Kaneko to represent the response of bound electrons, he also set relations that allow this function to represent the response of a free-electron gas (FEG) at $T = 0$, like in the case of conduction electrons in metals or valence electrons in semiconductors with small energy gaps. In this case, Kaneko [41] showed a correspondence between his WPM and Lindhard's FEG formulation [29], where the $\overline{q}$ parameter is connected with the electron gas parameter r_s by the relation $\overline{q} = 1.745/r_s$.

B. Extended wave-packet model

In a recent publication [43], we introduced the effect of energy binding in the wave-packet formulation using a method proposed by Levine and Louie (LL) [48]. This method consists of performing a shift in the frequency variable by the replacement, $\omega \to \sqrt{\omega^2 - \omega_s^2}$, where $\omega_s = I_s/\hbar$, and I_s is an energy gap which in the present case is the binding energy of a given atomic shell.

Specifically, the new dielectric function $\widetilde{\epsilon}$ becomes, for $\omega > \omega_s$,

$$\widetilde{\epsilon}_1(k,\omega) = \epsilon_1\left(k,\sqrt{\omega^2-\omega_s^2}\right), \tag{12}$$

$$\widetilde{\epsilon}_2(k,\omega) = \epsilon_2\left(k,\sqrt{\omega^2-\omega_s^2}\right), \tag{13}$$

whereas for $\omega < \omega_s$, $\widetilde{\epsilon}_2(k,\omega) = 0$, while $\widetilde{\epsilon}_1(k,\omega)$ is obtained from $\widetilde{\epsilon}_2(k,\omega)$ using the Kramers-Kronig relations. In this way, the LL method opens a gap in the map of excitations such that inelastic processes occur only for frequencies $\omega > \omega_s$. For this reason, all the quantities calculated here will be obtained from integrals in the domain $\omega > \omega_s$, where the values of $\widetilde{\epsilon}_1$ and $\widetilde{\epsilon}_2$ can be expressed analytically in terms of Eqs. (9)–(13). We refer to this approach as the *extended wave-packet model* (EWPM).

Finally, as is well known, the dielectric function of a free-electron gas satisfies specific sum rules. An important property of these models is that they also satisfy those sum rules [43,48].

C. Integrals for the energy-loss moments

The main moments of the energy-loss distribution are given by the following integrals (with $n = 0, 1, 2, \ldots$) [43,49]:

$$Q_n = \frac{2}{\pi}\left(\frac{Z_pe}{v}\right)^2\hbar^{n-1}\int_0^\infty\frac{dk}{k}\int_0^{kv}\omega^n\,\mathrm{Im}\left[\frac{-1}{\widetilde{\epsilon}(k,\omega)}\right]d\omega, \tag{14}$$

where $Z_p e$ and v are the charge and velocity of the incident particle. The units of Q_n are [energy]^n/length.

When $n = 0, 1$, and 2, this expression of Q_n yields the values of the inverse inelastic mean free path, stopping power, and energy straggling, respectively, i.e.,

(i) inverse inelastic mean free path (IMFP): $1/\lambda_i = Q_0$,

(ii) stopping power: $S = |\langle dE/dx\rangle| = Q_1$,

(iii) energy straggling: $\Omega^2 = \langle \delta E^2\rangle/dx = Q_2$.

In particular, the expression for the stopping power becomes

$$S = \frac{dE}{dx} = \frac{2}{\pi}\frac{Z_p^2 e^2}{v^2}\int_0^\infty \frac{dk}{k}\int_0^{kv} d\omega\,\omega\,\mathrm{Im}\left[\frac{-1}{\varepsilon(k,\omega)}\right]. \quad (15)$$

In the following, we will also refer to the "stopping cross section" (SCS) defined usually as SCS $= S/n_a$, where n_a is the target atomic density.

IV. WAVE-PACKET MODEL FOR PLASMAS

A. Extension of the dielectric model to quantum plasmas

In this section, we wish to perform a further extension of the wave-packet model with the purpose of describing, with the same formulation, the dielectric response of a plasma of free electrons in thermal equilibrium. This is a central question in order to achieve a unified description applicable to all targets. To accomplish this, we will make a connection between the full dielectric function of quantum plasmas described in Sec. II and the corresponding WPM described before. To establish this connection, we compare Eqs. (6) and (10), identifying the arguments of the corresponding exponential terms, as well as the prefactors in both expressions. This yields $u' = \sqrt{D}u = u/\theta^{1/2}$, $z' = \sqrt{D}z = z/\theta^{1/2}$, and

$$\frac{\sqrt{\pi}}{6}\frac{\chi_0^2}{\theta^{1/2}} = \frac{\pi\chi^2}{8}\theta^{3/2}. \quad (16)$$

And considering the definitions $u = \omega/kv_F$, $z = k/2k_F$, $u' = \omega/k\overline{v}$, $z' = k/2\overline{q}$, and $\chi_0^2 = 1/\pi k_F a_0$, we obtain the parameters for the plasma within the framework of the WPM:

$$\overline{q} = k_F\theta^{1/2},\ \overline{v} = v_F\theta^{1/2} \quad (17)$$

and

$$\chi^2 = \frac{4}{3\sqrt{\pi}}\frac{1}{\pi k_F a_0}\frac{1}{\theta^2}. \quad (18)$$

In this way, we obtain an analytical extension of the WPM dielectric function that represents the quantum behavior of free electrons in a plasma.

We now wish to show that the present formulation is able to describe the properties of the plasma on a very wide range of temperatures and densities. To show this, we will compare the results obtained with the present model with those of the exact dielectric function of a quantum plasma of Ref. [38].

First, it may be observed that this approach should yield the correct behavior for high enough temperatures, such that $k_B T \gg E_F$, where the use of Gaussian distributions for the electron speeds is most appropriate. The question then is to test the behavior of this model in the case of temperatures comparable to or smaller than E_F. In a previous work [50], it was shown that a Maxwell-Boltzmann type of approach can be extended down to temperatures close to E_F by replacing the actual temperature T by an effective temperature T^* corresponding to the mean-square velocity of the Fermi-Dirac distribution. Hinging on this idea, we searched for an extension of our model that could cover the complete range of temperatures, including low ($k_B T \ll E_F$) and high ($k_B T \gg E_F$) limits, as well as the transition range where $k_B T \sim E_F$.

To make this extension, we considered a quadratic interpolation between $k_B T$ and E_F of the form

$$k_B T_{eff} = \sqrt{(k_B T)^2 + \lambda E_F^2}, \quad (19)$$

where λ is a fitting parameter. The parameter θ in Eqs. (15) and (16) is now redefined as $\theta = k_B T_{eff}/E_F$. After a comprehensive set of comparisons, we found that the value $\lambda = 0.4$ allows a very satisfactory representation, on the whole range of temperatures, of the exact results obtained by other methods.

To illustrate this point, we show a set of comparisons in Fig. 1, for a quantum plasma with $r_s = 2$. For $T = 0$, we compare the results of this approach with those obtained from the degenerate FEG calculations using $\overline{q} = 1.745/r_s$, in accord with Kaneko's work [41], and with the Lindhard theory. For finite temperatures, the reference values are those obtained from the exact dielectric function of a quantum plasma, valid for all degrees of degeneracies, given in Ref. [38], which will be referred to as the AB theory.

The results shown in Fig. 1 cover different degrees of degeneracy, measured by the parameter θ. In Fig. 1(a), we show the case $T = 0$, i.e., a fully degenerate electron gas. Here we compare with the two sets of reference values for $T = 0$: Kaneko's WPM and the AB theory (which for $T = 0$ coincides exactly with the Lindhard theory). The main differences arise in the region of the stopping power maximum, where our calculation falls in between the two sets of reference points, providing a kind of average of those reference values. Figures 1(b)– 1(d) show additional comparisons for increasing values of the temperature. In these cases, the best reference values are those obtained with the exact AB theory. These panels shown that the results of the present model quickly approach those of the AB theory when $k_B T$ becomes close to or larger than E_F. In fact, for $k_B T \sim E_F$, the agreement with the AB results is excellent and becomes almost exact as T increases.

Therefore, we conclude that the present approach provides an excellent method to calculate the stopping power of plasmas for all degrees of degeneracy.

B. Effects of target ionization

As explained before, the main purpose of this study is to formulate a unified model to take into account the effects of target ionization on the energy loss and related precesses in dense media at high temperatures. Therefore, in the next section, we will consider various target elements of main interest assuming different degrees of ionization, starting from ground state at temperature $T = 0$ and then taking increasing values of both the temperature and the ionization degree. Under these conditions, we will calculate, on one side, the contribution of either filled or partially filled atomic shells and, on the other, the contribution of the surrounding plasma formed by

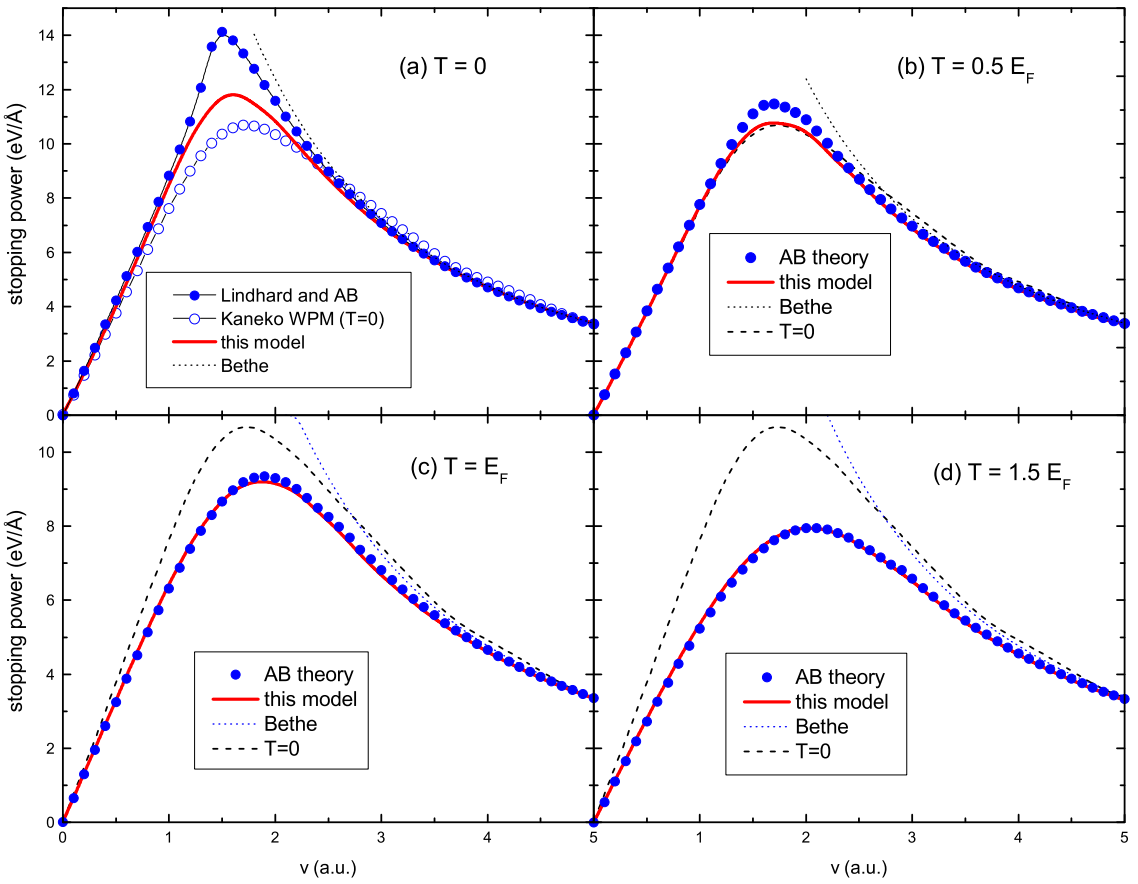

FIG. 1. Stopping power values calculated with the present approach (solid red lines) and comparisons with reference values for a quantum plasma with $r_s = 2$ and various temperatures. (a) Curve with solid circles: exact results calculated with Lindhard's dielectric function and with the AB theory (which coincides with the Lindhard function at $T = 0$); open circles: results of Kaneko's WPM model for a degenerate FEG. (b)–(d) Results obtained with the present approach (solid red lines) and with the AB theory (solid circles). The dashed line in these panels shows the WPM results for $T = 0$ only to illustrate the effect of the temperature with respect to these fixed values. The dotted curve shows the asymptotic limit given by the Bethe formula (which is independent of the temperature).

the electrons that have been thermally liberated from the target ion. All the calculations will be made using the unified scheme (UWPM) described before.

We will consider two alternative scenarios: First, we will assume particular ionization states where electrons are progressively removed from the atomic shells, leaving a target ion with charge Q and a plasma containing a number $N = Q$ of electrons per atom. Second, we will perform more comprehensive calculations to illustrate in a realistic way the effects of target ionization in conditions of thermal equilibrium.

V. UWPM CALCULATIONS

A. Stopping power for cold targets

Since the main energy-loss parameter, and also the most studied one both experimentally and theoretically, is the stopping power, the analysis here also refers to this quantity.

In Fig. 2, we show a comparison between the experimental results for the stopping cross sections for protons interacting with a cold Si solid target as a function of the projectile velocity [51] and the results calculated with our model. The contribution of the Si valence electrons (represented as a free-electron gas with $r_s = 2.01$) dominates the results for lower and intermediate velocities, while inner-shell contributions become increasingly relevant for intermediate and high

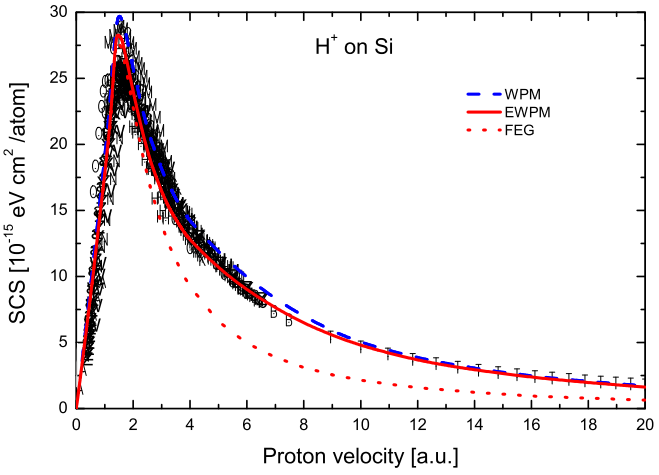

FIG. 2. Stopping cross section for protons on a cold Si target as a function of the projectile velocity. Dashed blue line: WPM; full red line: EWPM; dotted red line: FEG model with $r_s = 2.01$. Symbols: Experimental data extracted from [51].

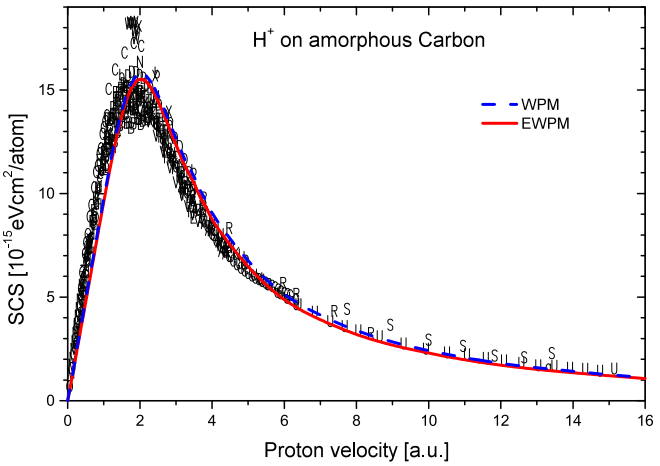

FIG. 3. Stopping cross section for protons on a cold C target as a function of the projectile velocity. Symbols: Experimental data extracted from [51].

velocities. As it may be seen, our model provides a good description of the stopping power on this extended energy range.

Additional calculations with this model are shown in Fig. 3 for a C target. As in the case of Si, the dominant contribution to the stopping is due to valence electrons, described as a free-electron gas with $r_s = 1.66$. In this case, the contribution of the only inner shell (i.e., the carbon K shell) is very small, so that no appreciable differences between the WPM and EWPM results are observed, and the FEG contribution nearly coincide with the total values. For low velocities, the theoretical results may still be improved by nonlinear calculations to take into account strong-interaction effects, as discussed in Ref. [43].

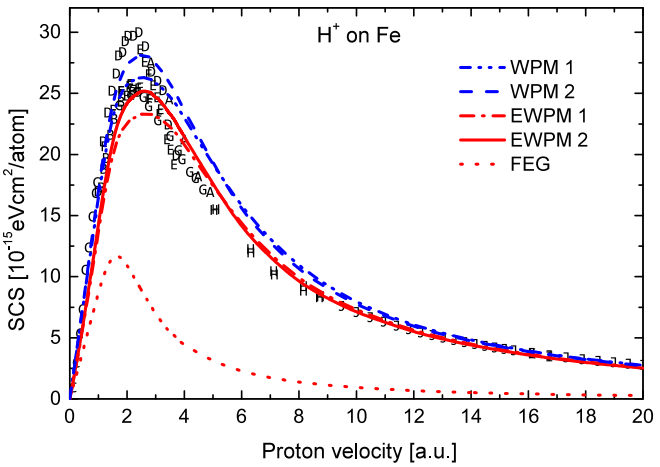

FIG. 4. Stopping cross section for protons on a cold Fe target as a function of the projectile velocity. Dash-dot-dotted blue line: WPM-1 calculated with the original parameters. Dashed blue line: WPM-2 calculated with a modified parameter for d electrons as described in the text. Dash-dotted red line: EWPM-1 model calculated with the original parameters. Solid red line: EWPM-2 model calculated with a modified parameter for d electrons as described in the text. Dotted red line: FEG with $r_s = 2.12$. Symbols: Experimental data extracted from [51].

Finally, our results for a Fe target are shown in Fig. 4. Here, we observe more significant differences between the WPM (blue line) and EWPM models, as a result of binding effects in the excitation of inner-shell electrons. In this case, we can make some additional considerations. As it has been discussed in the cases of Ag and Au in [43], d shells in transition metals show wider speed distributions than those obtained by Hartree-Fock calculations corresponding to free atoms. Consequently, EWPM coefficients corresponding to d-shell states should be modified. Contrarily to the previous two targets Si and C, as well as for standard metals such as Al, not containing d electrons, in the case of Fe and other transition metals the contribution of d electrons is dominant [43]. When this contribution increases, it produces an increment in the maximum of the stopping curve. This effect is shown in Fig. 4, which shows an improvement in the theoretical values around the maximum when we enhance the $3d$ Gaussian wave packet by modifying the corresponding coefficient from 0.963 (the value for free atoms [42]) to 0.8. On the other hand, significant discrepancies in the experimental values in the region of the stopping power maximum are observed in the three cases analyzed here (C, Si, and Fe). No clear consensus exists on which values should be considered more accurate.

B. Density and temperature changes

1. Partial analysis

The behavior of atoms or ions in plasmas can be characterized by the values of some relevant parameters, such as the ionization degree and the electronic density and temperature. In order to understand the individual role of these parameters in our model, we started analyzing the influence of a selected parameter on the calculated values while keeping constant the others. After this partial analysis, we considered a full description including all the simultaneous effects of target ionization and density and temperature changes. The tools used for the complete description include the use of the EWPM method applied to bound states, with consideration of the binding energy of each inner shell (which depends on the degree of ionization), and the use of the plasma model described in Sec. IV to take into account the contribution of the ionized electrons that form the surrounding plasma. This is what we call the unified model proposed in this work.

First we focus our analysis on the degree of ionization, defined as $i = N/Z$, where N is the number of ionized electrons and Z is the target atomic number, assuming in this case a cold target, without taking into account the effects of temperature or density variations. In Fig. 5, we show the stopping cross sections for the case of protons traversing cold targets of C, Si, and Fe, for different degrees of ionization. In this particular analysis, we have represented the free electrons as a degenerate electron gas, with $T = 0$, and characterized by Wigner-Seitz radii r_s appropriate to each case. To calculate r_s as a function of the degree of ionization, we have rescaled the r_s values corresponding to a solid target by a factor $(4/N)^{1/3}$ for C and Si, and $(2/N)^{1/3}$ for Fe. Thus, for instance, in the case of Si, we used $r_s = 2.01$ for $N = 4$, $r_s = 1.60$ for $N = 8$, $r_s = 1.39$ for $N = 12$, and $r_s = 1.32$ for $N = 14$. Although these N values are in this case arbitrary, the rationale of this example is in correspondence with the phenomenon of

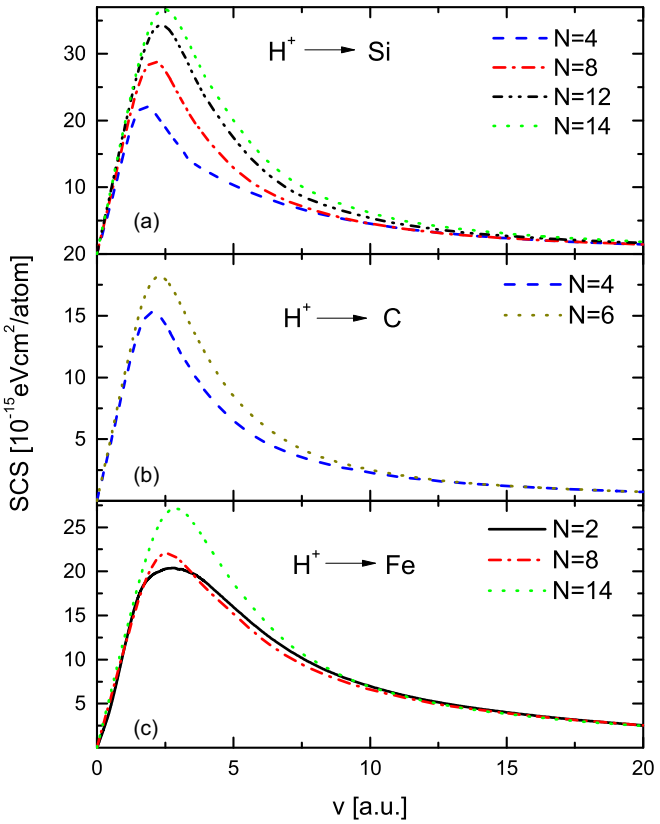

FIG. 5. Stopping cross section for protons on three different cold targets for several fixed degrees of ionization N as a function of the projectile velocity: (a) Si, (b) C, and (c) Fe.

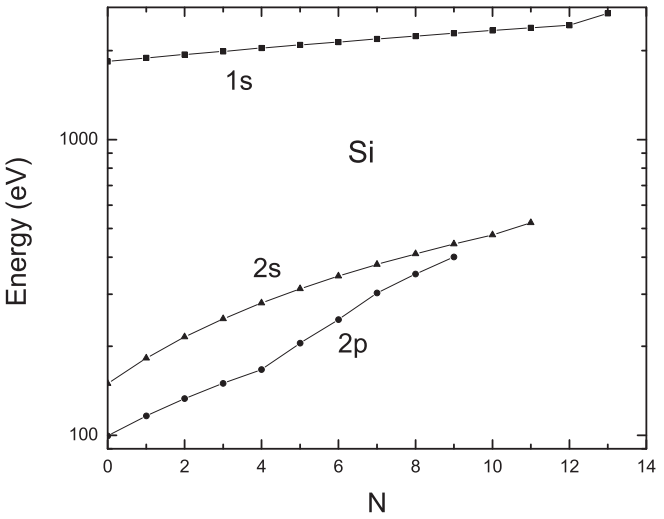

FIG. 6. Silicon ionization energies for levels $1s$, $2s$, and $2p$ as a function of the number of ionized electrons N, according to Ref. [56].

pressure ionization which occurs in cold matter subject to high pressures [52,53]. This phenomenon is of relevance in inertial-fusion studies [54] as well as in high-density stellar media [55]. As indicated before, the values of the inner-shell binding energies were readjusted according to the degree of ionization. The higher the degree of ionization, the lower the number of the remaining bound electrons, and the higher their binding energies. This effect is shown in detail in Fig. 6 for the case of Si, using the data obtained from NIST tabulations [56]. Consequently, the contribution of inner shells to the stopping decreases, while the contribution of the free electrons in the plasma increases. As a result of this, we find that the total stopping cross section increases with the degree of ionization as a consequence of the increment in the number of free electrons and the dominant free-electron contribution to the energy-loss process.

The case of Fe in Fig. 5 shows, however, a nontrivial behavior since the curves for $N = 2$ and $N = 8$ almost coincide. To understand this particular case, we show in Fig. 7 the separate contributions of the FEG and of the corresponding inner shells for the cases $N = 2$, 8, and 14 (more deeply bound shells are not shown since their contribution is negligibly small). Comparing the cases of $N = 2$ and $N = 8$, we observe a large growth in the FEG contribution, but it is compensated by the disappearance of the $3d$ contribution for $N = 8$. Simultaneously, we observe a significant decrease in the contribution of the $3p$ shell, which is produced by the increase in its binding energy (values of I_{3p}: 97.9 eV for $N = 2$, and 233.6 eV for $N = 8$). A similar reduction effect (although less significant), also produced by the increase of binding, occurs for the $3s$ contribution. Finally, for $N = 14$, there is a further increase in the FEG contribution (as the $3p$ shell contribution disappears), which yields almost the whole SCS value.

A different situation is shown in Fig. 8, where we show the total stopping cross section curves for a hot plasma for three different temperatures and a fixed value of target ionization, $N = 4$ for C and Si, and $N = 2$ for Fe. These values correspond to the removal of all the valence electrons in each target. Here we find a very fast decrease of the stopping with temperature in the cases of C and Si, and a milder one for Fe. This difference is due to the fact that C and Si have a smaller number of electrons in inner shells and hence a much larger contribution of valence or free electrons. This decrease with temperature is in accord with the similar behavior observed in the results for a pure plasma in Fig. 1 when $k_BT > E_F$. On the other hand, in the case of Fe, the contribution of inner shells is dominant, as may be observed in Fig. 4, and so in this case the total stopping power is less sensitive to changes in T.

Another relevant question of great interest for ICF or astrophysical studies is the effect of changes in the target density. In the case of ICF, the target is subject to the effects of internal compression and external ablation so that density values higher and lower than the normal ones are of interest. On the other hand, the interior of stars provides conditions of extreme densities and temperatures, and may include elements such as C, Si, and Fe, in various stages of the stellar evolution, as described in Sec. I. One of the advantages of the present formulation is that it may readily account for arbitrary (nonrelativistic) changes of the target density. To illustrate this point, we performed some additional calculations where we increased or decreased the density of the medium by arbitrary values.

In Fig. 9, we show the stopping cross section for protons impinging on a Si target for a fixed degree of ionization, but for different densities and temperatures. Here three temperatures were considered: $T = 30$, $T = 60$, and $T = 90$ eV; and

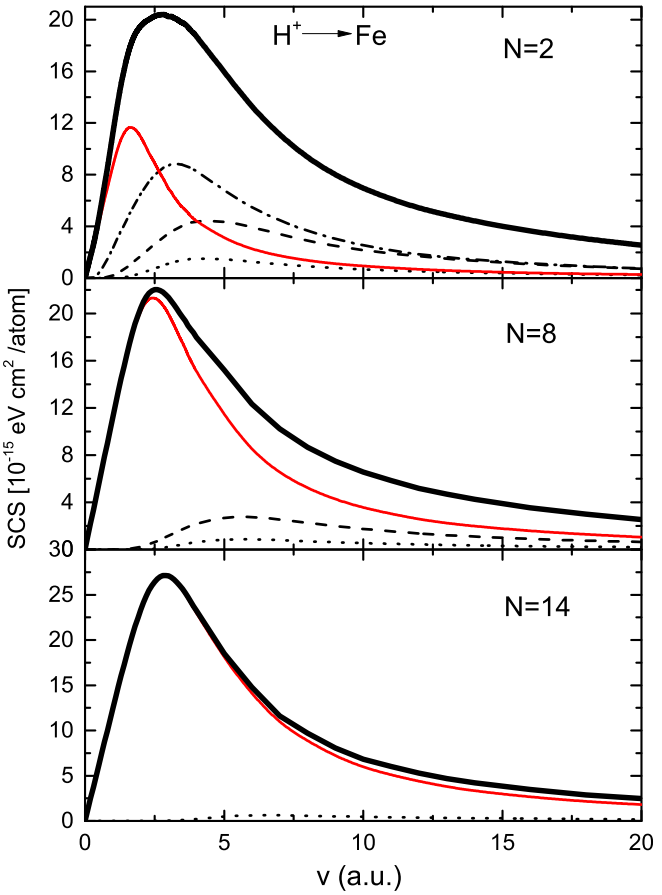

FIG. 7. Stopping cross-section contributions of levels $3s$, $3p$, and $3d$ of Fe, as a function of the projectile velocity, for $T = 0$ and for different numbers of ionized electrons N. Full thick line: total; full thin red line: FEG; dash-dotted line (only for $N = 2$): $3d$; dashed line (for $N = 2$ and 8): $3p$; dotted line: $3s$.

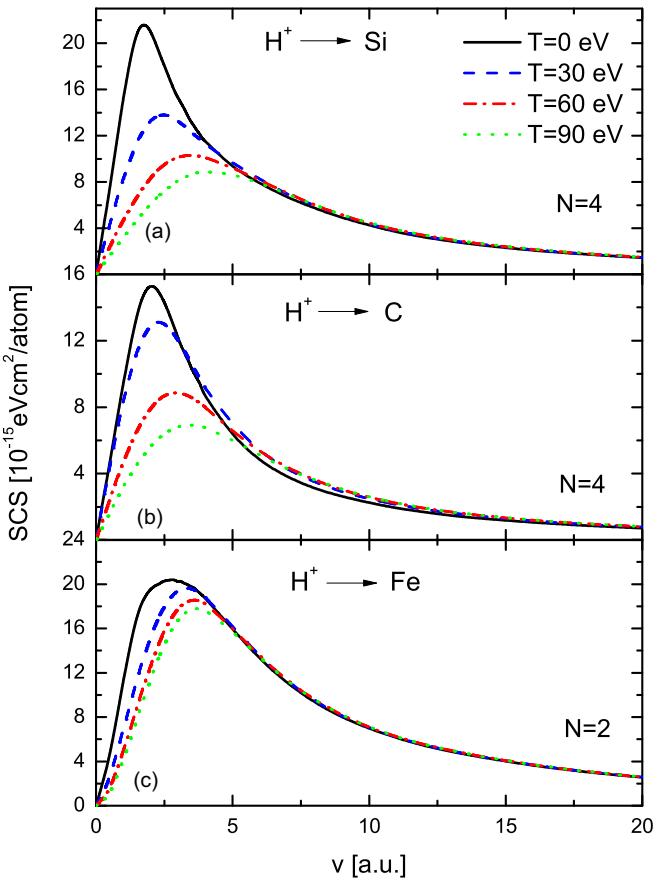

FIG. 8. Stopping cross sections for different temperatures and a fixed value of target ionized electrons N as a function of the projectile velocity: (a) Si, (b) C, and (c) Fe.

to evaluate the effects of changes in the target density, we considered three density values: $\rho_0/8$, ρ_0, and $8\rho_0$, taking as a value of reference the normal density of Si, $\rho_0 = 2.33\ \mathrm{g/cm^3}$.

Here we observe a seemingly contradictory behavior: the values for the target with increased density (blue lines) are smaller than those of the normal density (black lines), while the opposite is observed for the target with decreased density (red lines). However, if one analyzes the stopping power values, dE/dx, the behavior is the expected one: the higher the density, the larger the stopping power. This effect is particularly important at low energies and it has a simple but not obvious explanation: At low energies, the effect of screening by the free electrons is very important so that the stopping power S increases less than linearly with the density. As a result of this, S scales with $\sim n\ln(k_BT/n^{1/2})$, i.e., less than linearly with n, so that the stopping cross section, $\mathrm{SCS} = S/n_a = 4S/n$ in this case, decreases with n. (In the case of cold targets, one has to also consider the restrictions imposed by the Pauli principle which produces a similar effect [57].) In the opposite limit of high energies, S scales with $\sim n\ln(v^2/n^{1/2})$ and, in this case, the stopping cross section $\mathrm{SCS} = S/n_a$ converges to rather similar values when the logarithmic term becomes large [i.e., when $\ln(v^2/n^{1/2}) \gg 1$]. For still further details, the argument $v^2/n^{1/2}$ of the logarithm also explains why the curves for lower density (red lines) remain over the curves for higher density (blue lines) in Fig. 8.

To see the connection with the screening effect, we may recall that the logarithmic term depends in a general way on the ratio λ_s/λ_{qm}, where λ_s is a screening length and λ_{qm} is a typical quantum mechanical length. As described in Ref. [58], at low energies the screening length in a classical plasma ($\theta \gg 1$) is the Debye length $\lambda_D = [(k_BT/m)^{1/2}/\omega_p]$ and $\lambda_{qm} = \hbar/mv_T$, with $\omega_p = (4\pi ne^2/m)^{1/2}$ and $v_T = (k_BT/m)^{1/2}$, whereas at high energies, the screening weakens and λ_D is replaced by the adiabatic length $\lambda_{ad} = v/\omega_p$, while λ_{qm} is the de Broglie length $\hbar/mv$. It may be shown that these considerations explain very well the logarithmic behavior described before.

2. Calculations for thermal equilibrium

The final step in our analysis is to take into account, in a more complete way, the effects of the temperature on the particle-target interaction using an appropriate description of the target ionization in conditions of thermal equilibrium. In the previous examples, we have treated all parameters, i.e., density, temperature, and ionization degree, as if they were independent, but a realistic calculation should take into account that the degree of ionization increases with temperature, also considering the population distribution of charge states

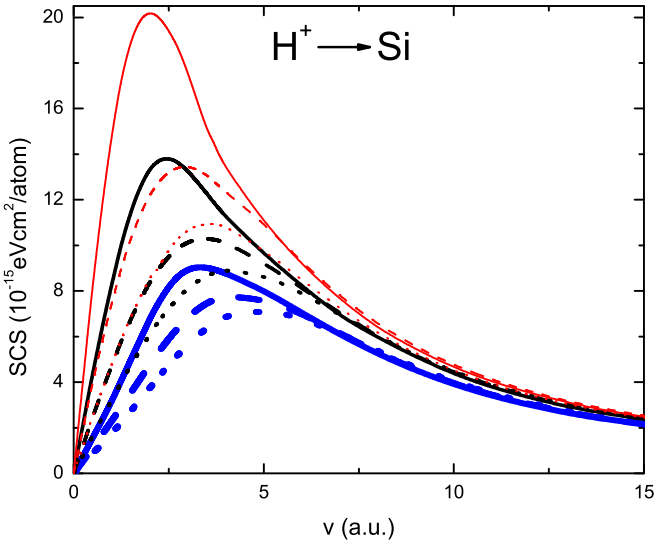

FIG. 9. Stopping cross section for protons on a Si target with a fixed degree of ionization $N = 4$ for different temperatures and densities, as a function of the projectile velocity. Black lines: normal density ρ_0; thick blue lines: $8\rho_0$; thin red lines: $\rho_0/8$. Full lines: $T = 30$ eV; dashed lines: $T = 60$ eV; dotted lines: $T = 90$ eV.

for each temperature. To describe these conditions in a proper way, we made use of the FLYCHK code [59], which is based on the Saha's equation [60], to calculate the population of the various atomic shells in conditions of thermal equilibrium at a given temperature T.

For each ionization state, a number N of electrons is extracted from the atom and incorporated into the surrounding plasma, so that its density increases with temperature. Hence, the free-electron contribution gradually becomes the dominant contribution to the stopping power as the temperature increases.

To illustrate these effects, here we consider the case of a Si target. The average number of electrons $\langle N\rangle$ transferred to the plasma obtained from the FLYCHK code is shown in Fig. 10(a), as a function of temperature T. Additionally, for each value of $\langle N\rangle$, the code delivers a distribution of charge-state values N. Using these values, we calculated the partial stopping power for each charge state and, finally, we obtained the statistical average of the stopping power for each temperature. The final results are the stopping cross sections shown in Fig. 10(b).

Figures 8 and 10 show some similarities in the temperature dependence; however, while Fig. 8 shows only particular cases, Fig. 10 shows the complete average corresponding to conditions of thermal equilibrium.

There is another aspect of interest that we may observe in Fig. 10: while the SCS values decrease in the low-velocity range, the opposite behavior is observed for v larger than about 5 a.u. This enhancement of the stopping power, produced by the thermal liberation of electrons by the target atoms, is in qualitative agreement with the experimental findings of Ref. [61], where significant enhancement of the energy deposition by very intense ion beams was observed. An additional effect that may contribute to a further enhancement of the energy loss in the experiment is the collisional ionization of the target due to the high intensity of the beam; this will

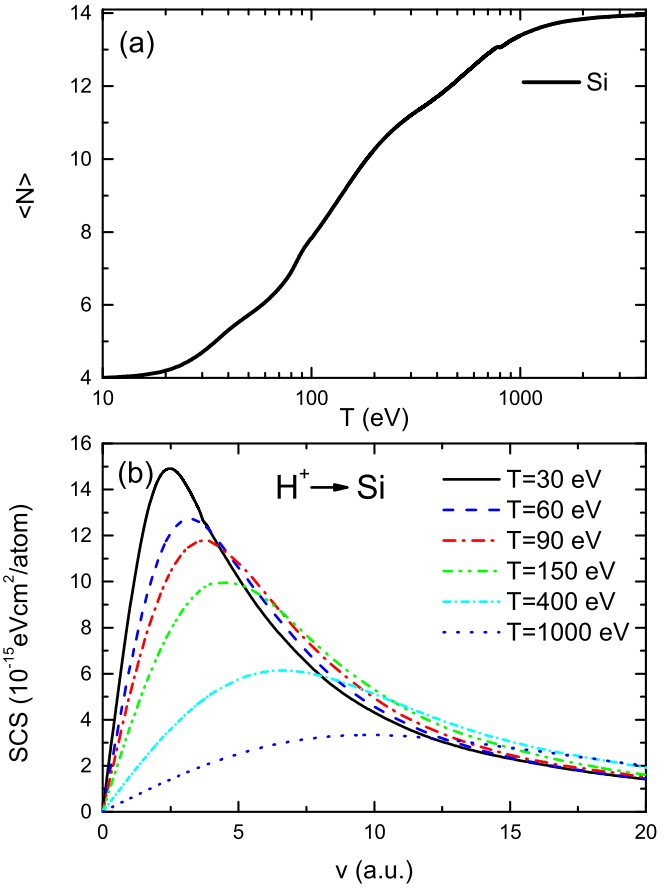

FIG. 10. (a) Mean ionization charge $\langle N\rangle$ as a function of temperature for a Si target with normal solid-state density according to the FLYCHK code [59]. (b) Stopping cross section for protons traversing a Si target for different temperatures as a function of the projectile velocity.

liberate additional electrons and will further increase the free-electron stopping power.

3. Application to stellar interiors

A second example, appropriate to conditions in the interior of aged stars in different moments of their evolution [25–27], is illustrated in Fig. 11. In this figure, we show results for the stopping cross sections (left scale) and stopping power (right scale) for protons in C, Si, and Fe, under conditions of very high densities and temperatures; in this case, for a density of 2.10^5 g/cm^3 and two temperatures: 45 and 86 keV (5.2×10^8 and 10^9 K, respectively). In these cases, the maximum of the stopping is displaced to much larger velocities, in the range of 70 to 90 a.u. Hence, due to the high speeds shown here, we must consider relativistic corrections. A full treatment of relativistic effects in the stopping power was made by Bethe, who derived the high-energy result [62–64],

$$S(v,\omega_p) = \frac{B}{v^2}\left[\ln\left(\frac{2mv^2\gamma^2}{\hbar\omega_p}\right) - \frac{v^2}{c^2}\right], \qquad (20)$$

where $B = 4\pi n Z_p^2 e^4/m$ and $\gamma(v) = 1/\sqrt{1 - v^2/c^2}$. This may be compared with the corresponding nonrelativistic

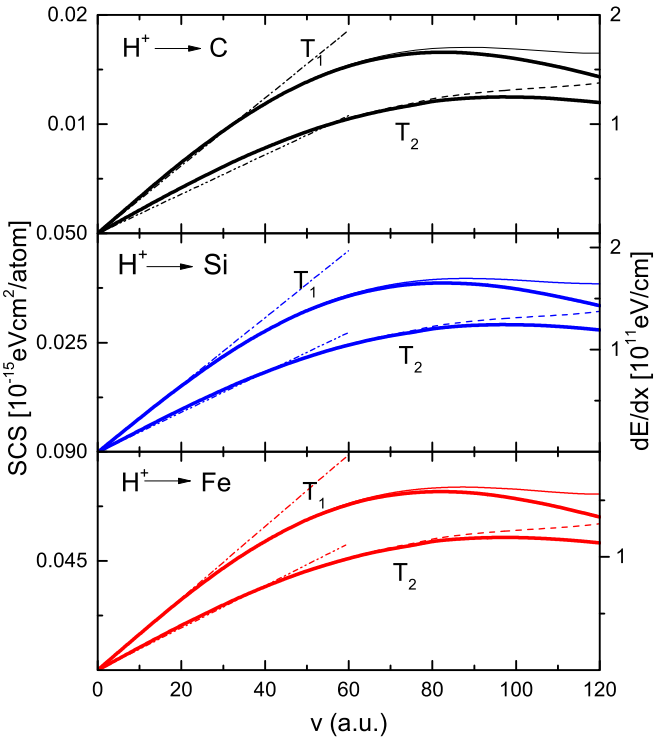

FIG. 11. Stopping cross section for protons traversing dense stellar regions with high temperatures, $T_1 = 45$ and $T_2 = 86$ keV, as a function of the particle velocity. Thin-solid and thin-dashed lines: relativistic corrections. Dash-dotted lines: analytical low-energy approximation of Eq. (23).

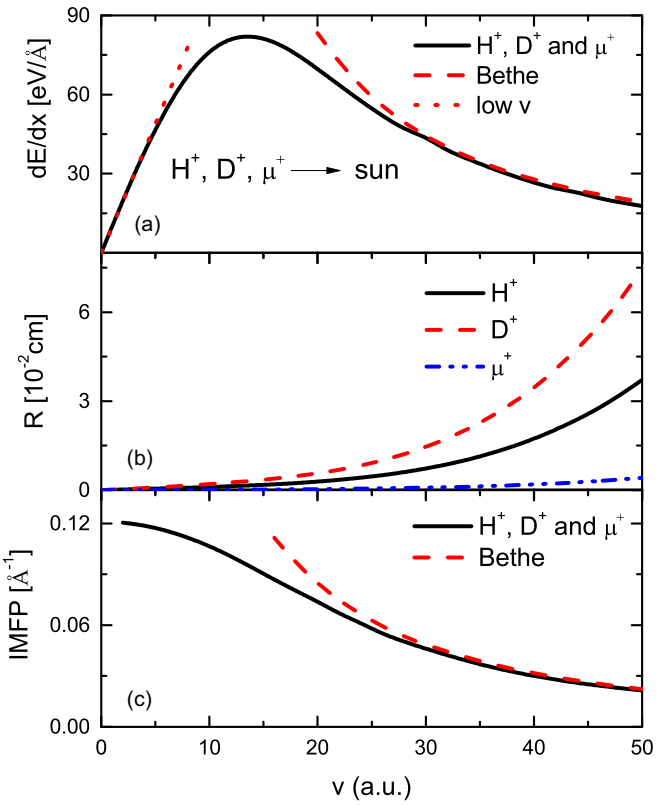

FIG. 12. Stopping power, range (R), and inverse mean free path (IMFP) for protons, deuterons, and muons moving within solar regions, for densities and temperatures corresponding to the sun center ($n_e = 8.4 \times 10^{25}$ cm^{-3}, $T_1 = 1.38$ keV), as a function of the projectile velocity.

expression

$$S_{nr}(v, \omega_p) = \frac{B}{v^2} \ln\left(\frac{2mv^2}{\hbar\omega_p}\right). \tag{21}$$

A compact form of the relativistic correction is given by the ratio of these two expressions, namely,

$$Q_{re}(v, \omega_p) = \frac{S(v, \omega_p)}{S_{nr}(v, \omega_p)}. \tag{22}$$

Since the relativistic effect is important only in the high-energy limit, we apply this correction by multiplying the stopping values calculated nonrelativistically by the correction factor Q_{re}. The departure of the relativistic stopping from the nonrelativistic one is illustrated in Fig. 11. We can see that the relativistic effects (curves shown by the dashed lines) start to be relevant for speeds larger that 80 a.u., although the magnitude of these corrections is not very large in the range that is explored (a maximum value of 20 percent at $v = 120$ a.u.).

On the other hand, the decrease of the stopping power values with temperatures in the low-velocity range, which is very notorious in the cases of highly ionized targets, such as in Figs. 10 and 11, may be explained very well using the approximation of Eq. (8) in the stopping integral of Eq. (15). This yields the following result for the low-energy behavior:

$$S = \frac{4}{3}\frac{(2\pi m)^{1/2}}{(k_B T)^{3/2}} Z_p^2 e^4 n v \left[\ln\left(\frac{k_B T}{\hbar\omega_p}\right) + \frac{1}{4}\right]. \tag{23}$$

This is the quantum mechanical version, obtained in Ref. [65], of a similar expression obtained previously by Spitzer [66] for classical plasmas. The decrease of S with T is basically a consequence of the dependence $1/T^{3/2}$ in the main term of this expression.

The straight lines in the lower-velocity range shown in Fig. 11 are the predictions of Eq. (23), calculated with the effective temperature values of Eq. (19). As may be observed, this "low-velocity" approximation yields excellent results for a very extended range of velocities. This shows that the validity range of this approximation is actually given by $v < v_{th}$, where $v_{th} = (k_B T/m)$ is a measure of the thermal speed of the plasma electrons. In the present cases, $v_{th} = 40.7$ and 56.2 a.u., for the temperatures of 45 and 86 keV of these calculations.

4. The case of solar interior

In order to further illustrate the wide range of applicability of the present method, we now consider the conditions in the region of the sun center, characterized by temperatures and densities of 16×10^6 K and 160 g/cm^3 respectively, and consisting of ≈75% hydrogen and 25% helium. This yields a total electron density of 8.4×10^{25} cm^{-3}.

In Fig. 12(a), we show the stopping power for protons, deuterons, and muons in the region of the sun's core. When plotted as a function of velocity, the stopping power is

the same for all these particles (since the isotopic effect is quite small) [67]. The maximum value of the energy loss is ∼80 eV/Å for velocities between 10 and 15 a.u. We may compare these values with more common cases of solids, such as Al or Si, where the maximum stopping values are of the order of 12–14 eV/Å for $v \sim 1.3$–2.0 a.u. There is a physical explanation for the shift in the stopping power maximum: this maximum occurs for velocities slightly larger than the thermal speed of electrons in the solar plasma (of the order of 10 a.u.), and of the Fermi speed in the case of cold solids (of the order of 1 a.u. for Al and Si).

The two lines shown in Fig. 12(a), for the low- and high-velocity ranges, are the analytical expressions of Eq. (23) (low-v approximation) and of the Bethe formula given by Eq. (21) (high-v approximation). As in the case of Fig. 11, we find that the low-velocity expression of Eq. (23) yields an excellent approximation. Together with the Bethe formula, both approximations very precisely explain the behavior of the stopping power in both limits.

Finally, another relevant quantity to characterize the energy-loss process is the distance traveled by the particles until they thermalize. To illustrate this, we show in Fig. 12(b) the penetration range of each of these particles, which is given by

$$R(E) = \int_{E_{th}}^{E} \frac{dE'}{S(E')}, \tag{24}$$

where $E_{th} = (3/2)k_B T$. This quantity shows a significant mass dependence (proportionality with particle mass), which produces the large split of proton, deuteron, and muon ranges shown in Fig. 12(b). These results may be scaled to other light bare ions, such as He^3 or He^4, by a factor M/Z_p^2, with M the mass and Z_p the atomic number of the particle. It may be parenthetically noted that the minimum value E_{th} in this integral might as well be taken as zero without any noticeable change in the range values (because of the comparatively large particle energies considered here).

5. Inverse mean free path

As a final example, we now consider the calculation of the mean free path of particles with the present method. This quantity is also of central interest for studies of energy transport in matter under various conditions, such as in all the systems considered before. Since the main aspects of the present approach have already been illustrated, here we will restrict our analysis to the case of charged particles moving in the interior of the sun, particularly in the region around the sun center, using the parameters specified before.

From the general form of Eq. (14), the inverse mean free path (IMFP) may be calculated by the integral expression,

$$\Lambda^{-1} = Q_0 = \frac{2}{\pi\hbar}\left(\frac{Z_p e}{v}\right)^2 \int_0^\infty \frac{dk}{k} \int_0^{kv} \mathrm{Im}\left[\frac{-1}{\tilde{\epsilon}(k,\omega)}\right] d\omega. \tag{25}$$

This quantity is shown in Fig. 12(c). The dashed line in this figure shows the asymptotic limit, given by a Bethe-like formula [49],

$$\Lambda^{-1} \cong \frac{(Z_p e)^2 \omega_p}{\hbar v^2} \ln\left(\frac{\alpha_0 v}{v_F}\right), \tag{26}$$

with $\alpha_0 = 1.5$ and $Z_p = 1$.

In this case (heavy particle), the IMFP has a maximum value at $v = 0$ [49], corresponding to a very short mean free path of $\Lambda \cong 8$ Å. The smallness of this value in comparison with the thermalization range R indicates that the typical energy transfer in each interaction, given by ΛS, is much smaller than the kinetic energy of the external particle. Thus, for instance, for $v = 10$ a.u. (energy of 2.5 MeV for protons), the typical energy loss per electronic interaction is $\Lambda S \cong 750$ eV; therefore, the slowing down of the projectile requires a very large number of interactions.

With this final example, we finish this set of calculations that was made to illustrate the application of the method to various systems subject to quite different physical conditions.

VI. CONCLUSIONS

Here we presented a unified approach to describe the interaction of charged particles with matter that applies to arbitrary values of densities, temperatures, and ionization state, covering the whole nonrelativistic range of densities and temperatures.

The model describes, with the same unified formulation, all the relevant target cases: (i) conduction or valence electrons in metals or insulators, (ii) bound electrons in atomic shells (solids and gases), and (iii) free electrons in plasmas. The method is especially appropriate to describe processes in neutral or ionized matter subject to extreme conditions of densities and temperatures.

We analyzed several cases of interest for fusion or astrophysical studies, considering in particular targets of special interest such as C, Si, and Fe, to illustrate the general applicability of the approach. The available experimental results for cold targets serve as a basic test of the approach, showing good agreement with the theoretical calculations. Moreover, the calculations yield an enhancement in the energy loss of swift ions in heated targets due to an increase in the number of free electrons, an effect that was experimentally observed.

The most significant advantage of the unified approach is, however, in the study of processes in very hot and dense media. In this study, we first illustrated the applicability of the theoretical scheme considering several arbitrary values of ionization states, densities, and temperatures, and, second, we applied the approach to realistic cases of thermal equilibrium. It should be noticed that the approach may be applied as well to arbitrary states of systems away from thermal equilibrium.

In summary, the method readily applies to any solid element in normal conditions, providing fairly good agreement with experiments; however, the possibility of including ionized plasmas and systems with arbitrary ionization states makes this approach most useful for applications to processes in ionized matter under extreme conditions of densities and temperatures. There is no other general method that could be applied in a straightforward way and with a unified formulation to the universe of cases indicated here.

ACKNOWLEDGMENTS

This work was supported by the following institutions of Argentina: Consejo Nacional de Investigaciones

Científicas y Técnicas and Agencia Nacional de Promoción Científica y Tecnológica. We especially acknowledge P. Grande for several useful comments and Y. Ralchenko for giving us the access to the FLYCHK code, as well as M. Barriga-Carrasco for very useful information.

[1] W. M. Wang, J. Roth, R. Behrisch, and G. Staudenmaier, Material transport at the vessel walls of the divertor tokamak ASDEX, J. Nucl. Mater. **162-164**, 422 (1989).

[2] S. S. Khirwadkar *et al.*, Fabrication and characterization of tungsten and graphite based PFC for divertor target elements of ITER like tokamak application, Fusion Eng. Des. **86**, 1736 (2011).

[3] https://en.wikipedia.org/wiki/Plasma-facing_material (unpublished).

[4] V. A. Abramov, First wall and divertor plate sputtering in a tokamak reactor, J. Nucl. Mater. **162-164**, 462 (1989).

[5] E. G. Hill and S. J. Rose, Modelling of silicon in inertial confinement fusion conditions, High Energy Density Phys. **8**, 307 (2012).

[6] E. M. Campbell *et al.*, Laser-direct-drive program: Promise, challenge, and path forward, Matter Radiat. Extremes **2**, 37 (2017).

[7] Z. Li *et al.*, Experimental investigation of Z-pinch radiation source for indirect drive inertial confinement fusion, Matter Radiat. Extremes **4**, 046201 (2019).

[8] C. Deutsch and G. Maynard, Ion stopping in dense plasmas: A basic physics approach, Matter Radiat. Extremes **1**, 277 (2016).

[9] C. Deutsch, Correlated ion stopping in dense plasmas, Matter Radiat. Extremes **4**, 034201 (2019).

[10] T. L. Mehlhorn, A finite material temperature model for ion energy deposition in ion-driven inertial confinement fusion targets, J. Appl. Phys. **52**, 6522 (1981).

[11] J. D. Lindl, R. L. McCrory, and E. M. Campbell, Progress toward ignition and propagating burn in inertial confinement fusion, Phys. Today **45**(9), 32 (1992).

[12] E. Nardi and Z. Zinamon, Charge State and Slowing of Fast Ions in a Plasma, Phys. Rev. Lett. **49**, 1251 (1982).

[13] A. Ng and A. R. Piriz, Ultrahigh-pressure generation using light-ion beams, Phys. Rev. A **40**, 1993 (1989).

[14] Z. Zinamon, E. Nardi, and M. Hass, Charge state fluctuations and energy loss straggling of fast ions in cold and in plasma targets, Nucl. Instrum. Methods Phys. Res. B **69**, 127 (1992).

[15] E. M. Bringa and N. R. Arista, Collective effects in the energy loss of ion beams in fusion plasmas, Phys. Rev. E **52**, 3010 (1995); Energy loss of correlated ions in plasmas: Collective and individual contributions plasmas, **54**, 4101 (1996).

[16] N. R. Arista and E. M. Bringa, Interaction of ion clusters with fusion plasmas: Scaling laws, Phys. Rev. A **55**, 2873 (1997).

[17] N. R. Arista, Stopping of molecules and clusters, Nucl. Instrum. Methods Phys. Res. B **164-165**, 108 (2000).

[18] A. R. Piriz, R. F. Portugues, N. A. Tahir, and D. H. H. Hoffmann, Implosion of multilayered cylindrical targets driven by intense heavy ion beams, Phys. Rev. E **66**, 056403 (2002).

[19] A. R. Piriz, R. F. Portugues, N. A. Tahir, and D. H. H. Hoffmann, Analytic model for studying heavy-ion-imploded cylindrical targets, Laser Part. Beams **20**, 427 (2002).

[20] E. Nardi, D. V. Fisher, M. Roth, A. Blazevic, and D. H. H. Hoffmann, Charge state of Zn projectile ions in partially ionized plasma: Simulations, Laser Part. Beams **24**, 131 (2006).

[21] E. Nardi, Y. Maron, and D. H. H. Hoffmann, Plasma diagnostics by means of the scattering of electrons and proton beams, Laser Part. Beams **25**, 489 (2007).

[22] Z. L. Miskovic, Y.-N. Wang, and Y.-H. Song, Dynamics of fast molecular ions in solids and plasmas: A review of recent theoretical developments, Nucl. Instrum. Methods Phys. Res. B **256**, 57 (2007).

[23] S. Heredia-Avalos, R. Garcia-Molina, and I. Abril, Energy-loss calculation of swift C_n^+ (n= 2–60) clusters through thin foils, Phys. Rev. A **76**, 012901 (2007).

[24] S. Heredia-Avalos, C. Denton, R. Garcia-Molina, and I. Abril, Simulation of swift boron clusters traversing amorphous carbon foils, Phys. Rev. A **75**, 012901 (2007).

[25] H. Reeves, *Stellar Evolution and Nucleo-Synthesis* (Gordon and Breach, Philadelphia, 1968).

[26] D. Clayton, *Principles of Stellar Evolution and Nucleosynthesis* (University of Chicago Press, Chicago, 1984).

[27] B. Paxton *et al.*, Astrophys. J. Suppl. Ser. **192**, 3 (2011).

[28] Typical densities in white dwarfs are in the range of 10^4–10^7 g/cm^3, while central densities may be as high as 10^8 g/cm^3; however, for densities beyond 10^6 g/cm^3, a relativistic model of dielectric response is required, including response to transverse fields not included in this study.

[29] J. Lindhard, On the properties of a gas of charged particles, Mat. Fys. Medd. Dan. Vid. Selsk **28**, 1 (1954).

[30] R. H. Ritchie, Interaction of charged particles with a degenerate fermi-dirac electron gas, Phys. Rev. **114**, 644 (1959).

[31] C. C. Montanari and J. E. Miraglia, The dielectric formalism for inelastic processes in high-energy ion-matter collisions, Adv. Quantum Chem. **65**, 165 (2013).

[32] D. Pines, Classical and quantum plasmas, J. Nucl. Energy, Part C Plasma Phys. **2**, 5 (1961).

[33] S. Ichimaru, *Basic Principles of Plasma Physics* (CRC Press, Boca Raton, FL, 1973).

[34] M. G. Calkin and P. J. Nicholson, Electrodynamics of a Semi-classical Free Electron Gas, Rev. Mod. Phys. **39**, 361 (1967).

[35] T. Peter and J. Meyer ter Vehn, Energy loss of heavy ions in dense plasma. 1. Linear and nonlinear Vlasov theory for the stopping power, Phys. Rev. A **43**, 1998 (1991).

[36] N. R. Arista and W. Brandt, Energy loss and straggling of charged particles in plasmas of all degeneracies, Phys. Rev. A **23**, 1898 (1981).

[37] G. Maynard and C. Deutsch, Energy loss and straggling of ions with any velocity in dense plasmas at any temperature, Phys. Rev. A **26**, 665 (1982).

[38] N. R. Arista and W. Brandt, Dielectric response of quantum plasmas in thermal equilibrium, Phys. Rev. A **29**, 1471 (1984).

[39] G. Maynard and C. Deutsch, Born random phase approximation for ion stopping in an arbitrarily degenerate electron fluid, J. Phys. **46**, 1113 (1985).

[40] T. Kaneko, Wave packet theory of bond electrons, Phys. Rev. A **40**, 2188 (1989).

[41] T. Kaneko, Partial and total electronic stoppings of solids and atoms for energetic ions, Phys. Status Solidi B **156**, 49 (1989).

[42] T. Kaneko, Partial and total electronic stopping cross sections of atoms and solids for protons, At. Data Nucl. Data Tables **53**, 271 (1993).

[43] C. D. Archubi and N. R. Arista, Extended wave-packet model to calculate energy-loss moments of protons in matter, Phys. Rev. A **96**, 062701 (2017).

[44] C. D. Archubi and N. R. Arista, Theoretical models to calculate stopping and ionization ratios of H2 molecules in solid targets, Phys. Rev A **99**, 032702 (2019).

[45] C. D. Archubi and N. R. Arista, Studies of threshold effects in the interaction of protons, electrons and positrons in matter using dielectric models, in *Rufus Ritchie, A Gentleman and A Scholar, Advances in Quantum Chemistry*, edited by J. Sabin and J. Oddershede (Academic Press, New York, 2019), Vol. 80, Chap. 10, pp. 247–269.

[46] A. D. McLean and R. S. McLean, Roothaan-Hartree-Fock atomic wave functions Slater basis-set expansions for $Z = 55$ to 92, At. Data Nucl. Data Tables **26**, 197 (1981).

[47] E. Clementi and D. Roetti, Roothaan-Hartree-Fock atomic wave functions: Basis functions and their coefficients for ground and certain excited states of neutral and ionized atoms, Z=54, At. Data Nucl. Data Tables **14**, 177 (1974).

[48] Z. H. Levine and S. G. Louie, New model dielectric function and exchange-correlation potential for semiconductors and insulators, Phys. Rev. B **25**, 6310 (1982).

[49] C. D. Archubi and N. R. Arista, A comparative study of threshold effects in the energy loss moments of protons, electrons and positrons using dielectric models for band gap materials, Eur. Phys. J. B **90**, 18 (2017).

[50] C. F. Clauser and N. R. Arista, Stopping power of dense plasmas, Phys. Rev. E **97**, 023202 (2018).

[51] Stopping power of matter for ions, graphs, data, comments and programs, https://www-nds.iaea.org/stopping/ (unpublished).

[52] D. S. Kothari, The theory of pressure-ionization and its applications, Proc. R. Soc. London A **165**, 486 (1938).

[53] R. M. More, Pressure ionization, resonances, and the continuity of bound and free states, Adv. At. Mol. Phys. **21**, 305 (1985).

[54] G. B. Zimmerman and R. M. More, Pressure ionization in laser-fusion target simulation, J. Quantum Spectrosc. Radiat. Transfer **23**, 517 (1980).

[55] F. C. Auluck, Mon. Not. R. Astron. Soc. **99**, 239 (1939).

[56] https://physics.nist.gov/PhysRefData/ASD/ionEnergy.html (unpublished).

[57] E. Fermi and E. Teller, The capture of negative mesotrons in matter, Phys. Rev. **72**, 399 (1947).

[58] L. de Ferrariis and N. R. Arista, Classical and quantum mechanical treatments of the energy loss of charged particles in dilute plasmas, Phys. Rev. A **29**, 2145 (1984).

[59] H. K. Chung, M. H. Chen, W. L. Morgan, Y. Ralchenko, and R. W. Lee, FLYCHK: Generalized population kinetics and spectral model for rapid spectroscopic analysis for all elements, High Energy Density Phys. **1**, 3 (2005).

[60] J. Larsen, *Foundations of High-Energy-Density Physics* (Cambridge University Press, Cambridge, 2017).

[61] F. C. Young, D. Mosher, S. J. Stephanakis, and S. A. Goldstein, Measurements of Enhanced Stopping of 1-MeV Deuterons in Target-Ablation Plasmas, Phys. Rev. Lett. **49**, 549 (1982).

[62] H. Bethe, Theory of the passage of fast corpuscular rays through matter (Zur Theorie des durchgangs schneller Korpuskularstrahlen durch materie), Ann. Phys. **397**, 325 (1930).

[63] U. Fano, Penetration of protons, alpha particles, and mesons, Annu. Rev. Nucl. Sci. **13**, 1 (1963).

[64] S. P. Ahlen, Theoretical and experimental aspects of the energy loss of relativistic heavily ionizing particles, Rev. Mod. Phys. **52**, 121 (1980).

[65] N. R. Arista, Low-velocity stopping power of semi-degenerate quantum plasmas, J. Phys. C: Solid State Phys. **18**, 5127 (1985).

[66] L. Spitzer, *Physics of Fully Ionized Gases* (Interscience, New York, 1956).

[67] J. E. Valdés, P. Vargas, and N. R. Arista, Differences in the energy loss of protons and positive muons in solids, Nucl. Instrum. Methods Phys. Res. B **174**, 9 (2001).